Developing a normative database for retinal perfusion using optical coherence tomography angiography

BINGYAO TAN,[1,2,3] YIN CI SIM,[3] JACQUELINE CHUA,[1,3,4] DHEO YUSUFI,[1,3] DAMON WONG,[1,2,3] AI PING YOW,[1,2,3] CALVIN CHIN,[4,5] ANNA C. S. TAN,[3,4,6] CHELVIN C. A. SNG,[3,7] RUPESH AGRAWAL,[3,8,9] LEKHA GOPAL,[10] RALENE SIM,[3] GAVIN TAN,[3,4] ECOSSE LAMOUREUX,[3,4] AND LEOPOLD SCHMETTERER[1,2,3,11,12,13,14,*]

[1] *SERI-NTU Advanced Ocular Engineering (STANCE), Singapore*
[2] *NTU Institute for Health Technologies, Singapore*
[3] *Singapore Eye Research Institute, Singapore National Eye Centre, Singapore*
[4] *Duke-NUS Medical School, Singapore*
[5] *National Heart Centre Singapore, Singapore*
[6] *Changi General Hospital, Singapore*
[7] *Department of Ophthalmology, National University Hospital, Singapore*
[8] *Tan Tock Seng Hospital, Singapore*
[9] *Lee Kong Chian School of Medicine, Nanyang Technological University, Singapore*
[10] *Khoo Teck Puat Hospital, Singapore*
[11] *School of Chemical and Biomedical Engineering, Nanyang Technological University, Singapore*
[12] *Department of Clinical Pharmacology, Medical University of Vienna, Austria*
[13] *Center for Medical Physics and Biomedical Engineering, Medical University of Vienna, Austria*
[14] *Institute of Molecular and Clinical Ophthalmology, Basel, Switzerland*
[*] *leopold.schmetterer@seri.com.sg*

Abstract: Visualizing and characterizing microvascular abnormalities with optical coherence tomography angiography (OCTA) has deepened our understanding of ocular diseases, such as glaucoma, diabetic retinopathy, and age-related macular degeneration. Two types of microvascular defects can be detected by OCTA: focal decrease because of localized absence and collapse of retinal capillaries, which is referred to as the non-perfusion area in OCTA, and diffuse perfusion decrease usually detected by comparing with healthy case-control groups. Wider OCTA allows for insights into peripheral retinal vascularity, but the heterogeneous perfusion distribution from the macula, parapapillary area to periphery hurdles the quantitative assessment. A normative database for OCTA could estimate how much individual's data deviate from the normal range, and where the deviations locate. Here, we acquired OCTA images using a swept-source OCT system and a 12×12 mm protocol in healthy subjects. We automatically segmented the large blood vessels with U-Net, corrected for anatomical factors such as the relative position of fovea and disc, and segmented the capillaries by a moving window scheme. A total of 195 eyes were included and divided into 4 age groups: < 30 (n=24) years old, 30-49 (n=28) years old, 50-69 (n=109) years old and >69 (n=34) years old. This provides an age-dependent normative database for characterizing retinal perfusion abnormalities in 12×12 mm OCTA images. The usefulness of the normative database was tested on two pathological groups: one with diabetic retinopathy; the other with glaucoma.

1. Introduction

Optical coherence tomography angiography (OCTA) is a three-dimensional, non-invasive, and dye-free vascular imaging modality that outperforms injection-based retina vascular imaging modalities, such as fluorescein angiography and indocyanine green angiography in many aspects. OCTA can visualize, characterize and quantify the vascular abnormalities in macular and parapapillary regions in a broad spectrum of ocular diseases including glaucoma, diabetic retinopathy (DR), and age-related macular degeneration [1–4].

The recent development of OCTA with wide-angle optics design, fast acquisitions, better registration algorithms, and eye tracker incorporations, has provided insights into the pathological vascular alteration in the posterior pole [5–9]. For instance, it showed higher diagnostic power in stratifying non-proliferative DR (NPDR) compared with the narrower macular scan for the reason that initial retinal capillaries dropout could happen in the retinal periphery [6]. Focal retinal perfusion defects reflected by localized absence or collapse of the capillaries could be easily identified as areas of non-perfusion in OCTA, and diffused retinal perfusion decrease was usually detected by comparing with age-matched case-control groups. Therefore, normative databases played an important role in differentiating and grading the vascular abnormalities, especially for the diffused capillary defects. A few studies have reported the normative OCTA database in the macula or parapapillary regions [10–12]; however, developing a normative database in 12×12 mm is more challenging because of several obstacles, including perfusion density heterogeneity among macular, parapapillary to peripheral regions, and uneven illumination resulted from optical vignetting.

Here for the first time, we developed a normative database for retinal perfusion density using 12×12 mm OCTA. Images were acquired on a swept-source OCT (SS-OCT) prototype (PlexElite 9000, Zeiss Meditec, Dublin, CA, USA). Large vessels were automatically isolated using a validated U-Net, and the entire database was divided into 4 age groups: < 30 years old, 30-49 years old, 50-69 years old and >69 years old. We also demonstrated the usefulness of the normative database in quantifying the retinal perfusion change in eyes with primary open-angle glaucoma (POAG) and NPDR.

2. Methods

2.1. OCTA protocol

This is a prospective study. Normal subjects were recruited from three cohorts (PIONEER: The PopulatION HEath and Eye Disease PRofile in Elderly Singaporeans; SIENA: the Singapore Imaging Eye Network; and REMODEL: Response of the Myopcardium to Hpertrophic Conditions in the Adult Population) from Singapore National Eye Center (SNEC) outpatient clinics during the period of January 2018 to January 2020. Inclusion criteria for the healthy subjects were no evidence of hypertension or ocular pathologies, including glaucoma, DR, and age-related macular degeneration. Another two groups of participants (n = 20) were included to evaluate the normative database: POAG participants were recruited from the SIENA protocol, and NPDR participants were recruited from Diabetes study in Nephropathy And other Microvascular complications protocol. These studies were approved by the SingHealth Centralized Institutional Review Board and conducted in accordance with the Declaration of Helsinki. Written informed consent was obtained from every participant.

OCTA images were taken using a prototype SS-OCT system operated in 1050 nm region and 100 nm bandwidth. The system operated at a speed of 100,000 A-scans/second, and the axial and lateral resolutions in tissue were 6.3μm and 20μm, respectively.

A 12×12 mm scanning protocol centered at the fovea was applied, and each volume consisted of 500 A-scans and 500 B-scans. Each B-scan was repeated twice for generating OCTA images using an optical microangiography algorithm [13]. Motion related artifacts were minimized

by an integrated line scanning ophthalmoscope (LSO) eye tracker during data acquisition. A review software (Zeiss Meditec, Dublin, CA, USA) provided the automated segmentation of retinal layers and retinal pigment epithelium (RPE). The segmentation was carefully checked, and manual corrections were applied when necessary. Superficial capillary plexus (SCP, inner limiting membrane – inner plexiform layer) and deep capillary plexus (DCP, outer plexiform layer) with automatic projection removal were extracted for further analysis. The exported images were interpolated to 1024×1024 pixels. The signal strength index (SSI) as an indication of the image quality was also extracted.

2.2.   The validation of automated large vessel isolation via deep learning

Large retinal vessels were automatically segmented with U-Net [14]: a fully-convolutional deep learning architecture widely applied in segmenting biomedical images. The U-Net was characterized by a downsampling path and an upsampling path. In the downsampling path, stacks of convolutional, max pooling layers and activation units captured the context from the image; in the upsampling path, transposed convolutions upsampled the features. Skip connections concatenated the feature maps at the same scale to provide location information. In the end, a single channel convolution, together with batch normalization and sigmoid activation function, calculated a probability map, which was converted into a binarized map with a predefined threshold (0.5). The diagram of the U-Net and the detailed parameters are shown in Fig. 1.
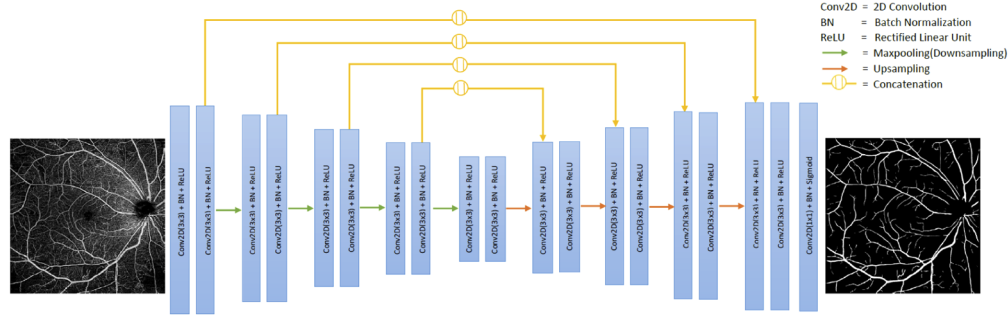

Fig. 1. U-Net architecture for large vessel segmentation in OCTA images.

Large vessels were manually delineated by two graders, where the overlap was regarded as the ground truth. The annotation of large vessels is based on whether the tubular structure of the vessel can be recognized. We trained the U-Net over 80 12×12 mm OCTA images from a separate database using a custom made IoU (Intersection over Union) loss function as shown in Eqn. (1), where y^{pred} was the predicted binarized matrix, y^{true} was the ground-truth, and i,j were the coordinate indicators.

$$L_{IoU} = 1 - \frac{\sum_{i,j \in N} y_{i,j}^{pred} y_{i,j}^{true}}{\sum_{i,j \in N} y_{i,j}^{pred} + y_{i,j}^{true} - y_{i,j}^{pred} y_{i,j}^{true}} \tag{1}$$

A five-fold cross-validation method was used to evaluate the architecture, the best of which was applied to segment the large vessels [15]. An original 12×12 mm OCTA image and its corresponding U-Net segmented large vessel masks are shown in Fig. 2(A-B), and overlaid vessel mask and OCTA image illustrated the accuracy of large vessel segmentation (Fig. 2(C)).

We further evaluated the model with several scores:

IoU score: The area of intersection between predicted and ground-truth maps divided by area of union.
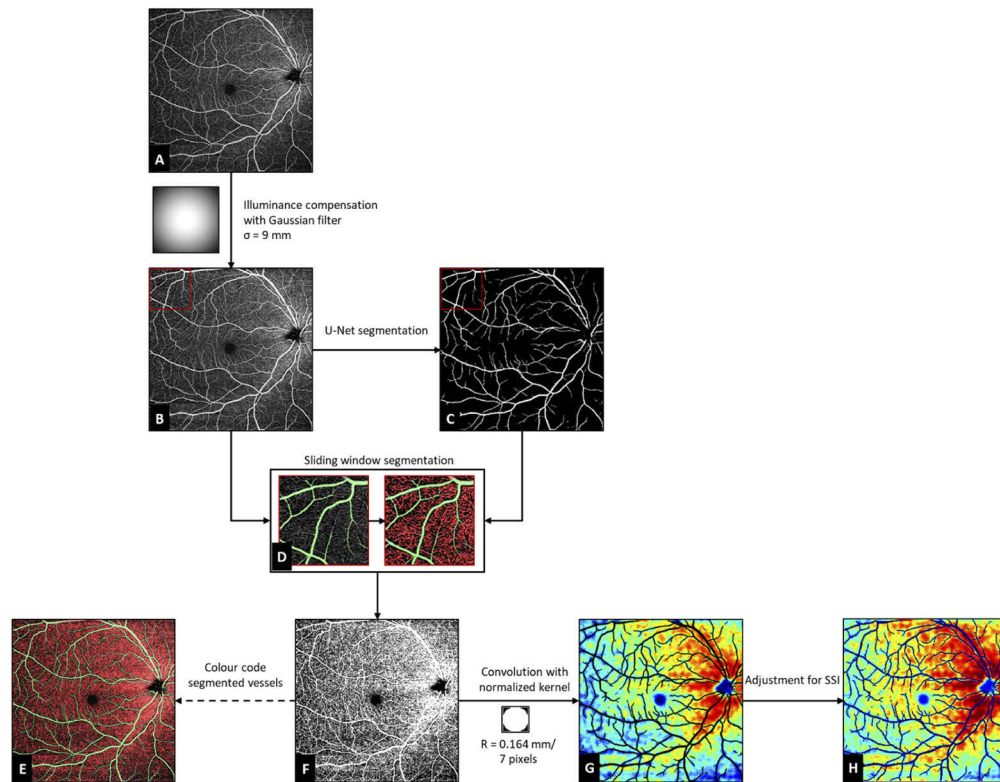
Fig. 2. Process flow diagram for generation of capillary perfusion density maps. A) A representative 12×12 mm OCTA image (Male, Age: 60, SSI: 8) on superficial capillary plexus. B) OCTA image after illuminance compensation with Gaussian filter. C) Large vessels segmented by U-Net. D) Capillary segmentation in a window with size 3×3 mm. E) Color coded retinal vessel map with green and red representing large vessels and capillaries, respectively. F) Binarized 12×12 mm retinal vessel map using a sliding window segmentation scheme. Capillary perfusion density maps before (G) and after signal strength index (SSI) adjustment. Shown in *jet* colormap. Large vessels were masked out in black.

Dice score: 2X area of intersection between predicted and ground-truth maps divided by the sum of areas of these two maps.

Accuracy score: percentage of the correctly predicted areas.

2.3. Perfusion density heatmap

A custom MATLAB (MathWorks Inc, MA, USA) algorithm was developed to generate a map representing microvascular perfusion density in SCP, DCP, and total retinal vasculature of healthy adults. It comprised the following steps. Firstly, to compensate for decreased illuminance at the peripheral regions of the 12×12 mm OCTA, we divided the OCTA image by a rotationally symmetric Gaussian lowpass filter (sigma = 9 mm). A sliding window scheme (window size: 3×3 mm; sliding step: 0.375 mm in both directions) was used to segment the capillaries and compensate for the residual uneven illuminance. In each window, the threshold was empirically set as 40% of the mean intensity of large vessels, and the threshold was applied to all superficial, deep, and full retinal angiograms. All the vessels in DCP were considered as capillaries. Binarized images were therefore generated, where the regions with large vessels and capillaries were set to 1, while the background was set to 0 (Fig. 2(D)). A binarized perfusion map with large

vessel selectivity is shown in Fig. 2(E). Red and green colors represented capillaries and large vessels, respectively. Secondly, to calculate the capillary perfusion density, the values of large vessel regions were set to Not a Number (NaN). Lastly, the perfusion map was calculated as the convolution between a normalized kernel (a disk-shaped structuring element, radius = 0.164 mm) and the binarized capillary images, omitting NaN values. The perfusion map was converted to a *jet* color scale heatmap as shown in Fig. 2(F). The correlation between perfusion density and SSI were fit in a linear function, and perfusion density from individual map was adjusted based on its SSI and the average SSI over the entire database, as shown in Fig. 2(H).

To register individual maps, centers of the fovea and optic nerve head (ONH) were automatically identified. Fovea center was referred to as the geometrical center of the fovea avascular zone, and ONH was segmented by simply searching for the non-perfused regions in nasal parts of the image. The distance and the tilt between the fovea and ONH centers were calculated on individual maps. Consequently, the mean locations of the fovea and ONH centers were computed and served as the reference as shown in Fig. 3. Individual maps were registered to the reference via nonreflective similarity transformation, where both ocular magnification and tilt were partially compensated. Average and standard deviation (SD) maps were calculated to show the distribution of capillary perfusion density across a wide field. The capillary defect map calculated the difference between the age-match averaged capillary perfusion map and the registered capillary perfusion map of individuals, normalized by the SD.
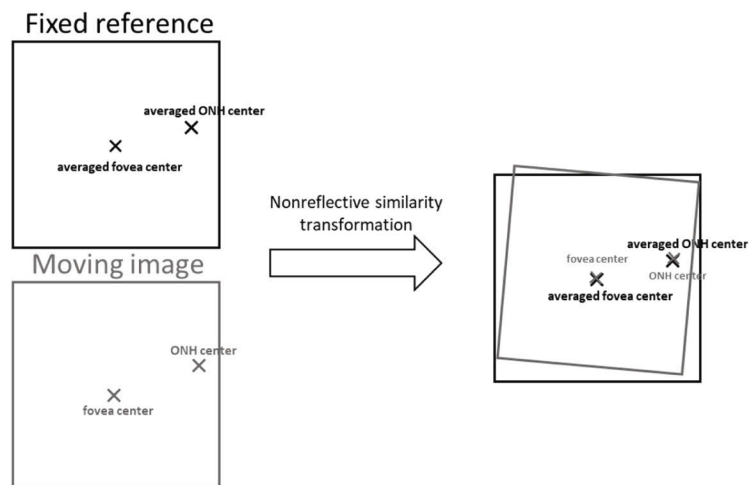

Fig. 3. Illustration of geometric non-rigid registration to compensate for magnification and tilt. ONH: optic nerve head.

We also extracted the perfusion density in three regions of interest: a 6×6 mm region centered at the fovea, the remaining square annulus, and the entire field of view (12×12 mm). Perfusion density was calculated as the ratio between the area with microvasculature per total area excluding large vessels.

3. Results and discussion

3.1. U-Net on the accuracy of automated large vessel segmentation

Despite different IoU scores, major arteries and veins were accurately segmented by U-Net (Fig. 4), whereas the disagreement between predicted and ground-truth maps was mainly on arterioles and venules. High accuracy score (97.67%) indicated that major vessels were fully

picked up by the U-Net, while the slight under-segmentation of the arterioles and venules were likely due to their insufficient differentiation from capillaries in OCTA images and inconsistent ground truth annotations (Intergrader IoU: 87.42%, Dice: 93.26%).
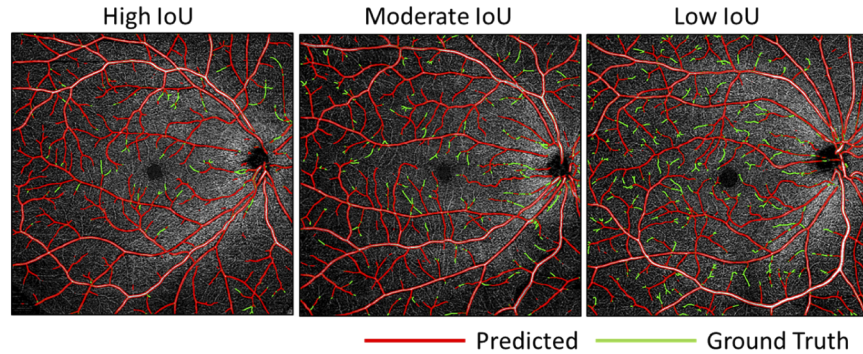

Fig. 4. Representative large vessel segmentation results with high, moderate, and low IoU scores. Different scores (IoU, Dice, Accuracy) were calculated to evaluate the performance of the U-Net, as well as the repeatability between graders. IoU: Intersection over Union.

For the most adopted Frangi [16] and Gabor filters [17], enhancing the vessels with one scale could interfere with vessels in other scales [18]. For the recent Bayesian residual transform, information on the image is decomposed into independent scales, but prior knowledge of the scale range is essential [19]. In contrast, U-Net could simultaneously and accurately segment the large vessels with a broad scale range and performed better on complex vascular structures including vessel branching, crossing, and even ONH. The performance of segmentation with Frangi (sigma: 2-6 pixels), Gabor (theta: 16 orientations from 0-pi; frequency: 0.1-0.2 pixel; sigma: 2-6 pixels) or both filters is shown in Fig. 5 and summarized in Table 1. Parameters were optimized by maximizing IoU. Visually U-Net performed the best, where Gabor filter over-segmented the highly reflective parapapillary regions, and the Frangi or Gabor + Frangi filter yielded some disconnection at vessel branches and crosses. U-Net achieved the highest IoU, Dice score and accuracy score. The accuracy of the large vessel segmentation is not only important to the following capillary segmentation and quantification, but also valuable for future studies on vessel calibers in patients with systemic diseases [20].
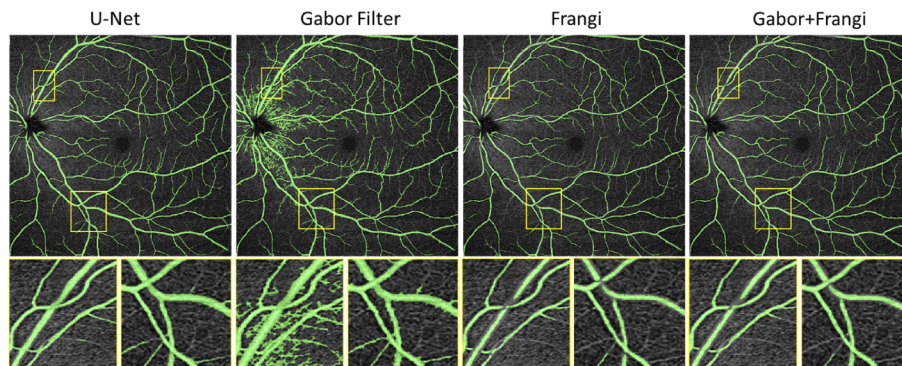

Fig. 5. Comparison between U-Net and traditional vessel enhancement algorithms.

Table 1. Large vessel segmentation performance

	Inter-grader	Frangi	Gabor	Gabor + Frangi	U-Net
IoU	87.42%	69.79%	57.95%	75.02%	**78.65%**
Dice	93.26%	82.20%	73.31%	85.71%	**87.50%**
Accuracy		89.05%	73.01%	85.06%	**97.67%**

3.2. Age-dependent average and SD perfusion maps

A total of 195 eyes from 138 (Male = 92; Age: 58.8±15.1 years old, range 23-89 years old, SSI: 8.70±0.88) Asian subjects were included, with 24 eyes in group 1 (<30 years old, age: 25±2.4 years old, SSI: 9.04±0.69), 28 eyes in group 2 (30-49 years old, age: 44.2±3.9 years old, SSI: 8.75±0.93), 109 eyes in group 3 (50-69 years old, age: 60.8±5.8 years old, SSI: 8.60±0.88), and 34 in group 4 (>69 years old, age: 75.8±5.0 years old, 8.76±0.96). All the scans were strictly checked to ensure high quality (SSI>7), and SSI was not significantly different between groups (p = 0.15, analysis of variance). The correlation between perfusion density in each plexus and SSI are shown in Supplementary Figure 1, and as mentioned in the method section, the all the perfusion density reported here are after SSI adjustment.

The average and SD capillary perfusion maps, that were adjusted for SSI, from three layers (SCP, DCP, and full retina) are shown in Fig. 6. Visually, the spatial distribution of mean perfusion density in SCP was similar to the one of the retinal nerve fiber layer (RNFL) thickness, indicating a strong association between vascular and axonal support to the retinal ganglion cells [21,22]. The capillaries in DCP were evenly distributed over the entire region, where parapapillary regions (Fig. 6, black arrows) have relatively higher perfusion density. This is in keeping with others' reports [23–25] and might due to the insufficient performance of the segmentation and projection removal algorithms. For the SD maps, optic disc size variation among individuals caused ring-shaped structures around the ONH (Fig. 6, white arrows) [26]. Low SD in the parapapillary regions (Fig. 6, orange arrows) is correlated with the high capillary perfusion, while high SD were mostly in the peripheral regions (Fig. 6, red arrows), especially interior-nasal and superior-nasal regions. Several potential hypotheses could explain this high peripheral perfusion variation, including individual capillary perfusion difference between individuals, optical vignetting due to eye aberration, and the variation of FOV that was partially compensated. Both average and SD maps need to be considered to determine the deviation from the normal range.

The overall spatial distribution patterns were similar among the three age groups. Notably, capillary density progressively decreased in the regions superior and inferior to the macula in both SCP and full retina, and the perfusion density in the peripheral regions was significantly lower in the age group >69 years old. Moreover, the SD in SCP and full retina increased over the ages, reflected by shrinkage of the low SD area (blue color regions) and expansion of the high SD area (red color regions). Interestingly, the SD in DCP was highest in the age group between 50-69 years. This might be explained by a relatively fast decline rate of the perfusion in DCP in this age group, while the rate differed among individuals [27,28].

To investigate the age-dependent retinal perfusion in more detail, we simulated the retinal nerve fiber trajectories based on a mathematical model proposed by Jansonius et al. [29,30] and studied the age-dependent perfusion density change along these trajectories. Figure 6(A) showed a SCP perfusion map in linear grayscale, where the black curves represented the trajectories from the ONH, separated by 10 degrees. Finer trajectories were plotted with 1-degree separation and the distance to the ONH along the trajectory was calculated and represented in *parula* color scale. The perfusion density along the fine trajectories was plotted in Fig. 7(B-D). Solid curves and the semi-transparent bands represented the mean and the SD of perfusion along the trajectories, respectively. The perfusion density ranged between 30-57% in SCP, 22-34% in DCP, and 36-62% in full retina. It decreased monotonically from parapapillary towards the periphery in SCP and
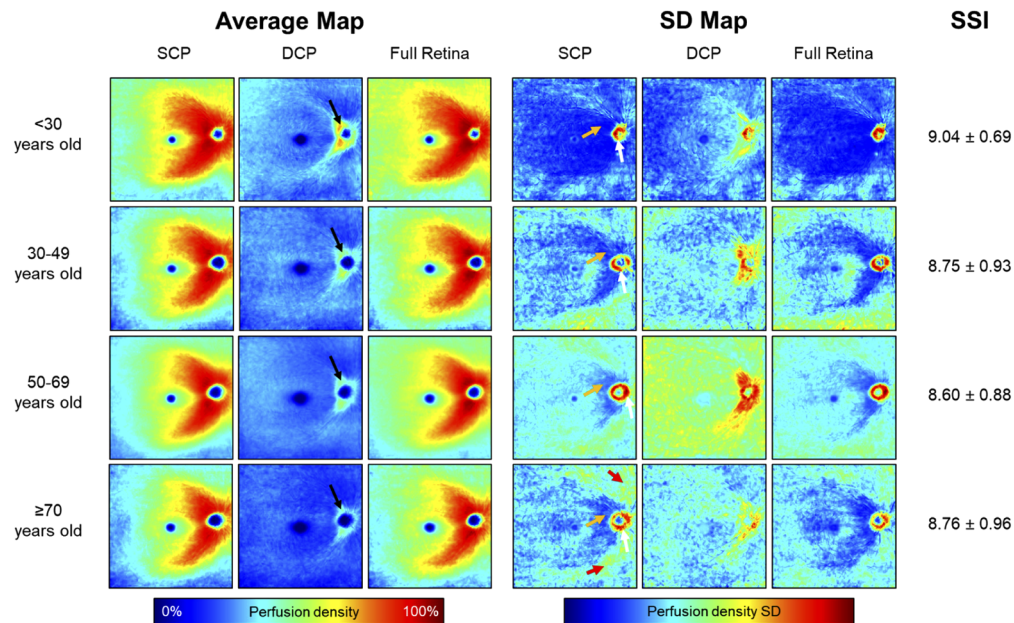
Fig. 6. Average and standard deviation (SD) perfusion maps from three ages groups.

total retina but fluctuated in DCP. The absolute perfusion density values are highly dependent on system parameters including laser wavelength, lateral resolution, sampling resolution, and B-scan rate, as well as post-processing parameters including threshold method [31–34]. Nevertheless, the age-dependent perfusion density decrease in SCP and full retina was predominant in younger ages, but in DCP was in older ages In older ages (>50 years old), the age-dependent decrease in perfusion was more predominant in DCP than in SCP, which is in agreement with previous studies [28,35]. Although no clear evidence showed the nourishing relationship between DCP and specific neurons, we hypothesize that DCP provides oxygen and nutrients to horizontal and bipolar cells. Different neurons could undergo heterogeneous aging journeys [36], but deep neurons may be more susceptible to aging than the superficial neurons (retinal ganglion cells and amacrine cells), occurring first in the parapapillary area and then later in the peripheral area. Further studies are, however, required to experimentally verify this hypothesis.

3.3. Clinical application of the normative database in various eye diseases

The normative database could provide an intuitive observation of microvascular changes in a variety of eye diseases. A direct defect map could inform the ophthalmologists with the loci and severities of microvascular alterations, in a wide field of view. Next, we applied the normative datasets on two types of common eye diseases, namely, POAG and NPDR.

Two representative eyes from the same male patient (age: 37 years old) illustrated the identification and characterization of the glaucomatous damage in microvasculature using the normative database. The visual field tests showed early arcuate [37] loss along with the nerve fiber bundles in both superior and inferior hemifields (Fig. 8(A)) in the right eye, and in superior hemifields (Fig. 8(E)) in the left eye. The right eye was categorized as mild glaucoma (pattern deviation: −2.85 dB) and left eye was categorized as pre-perimetric glaucoma (pattern deviation: −1.69 dB) [38]. Low perfusion arcuate bands along the nerve fiber trajectories could be visualized from the grayscale OCTA image as well as its capillary perfusion map (SSI: 10 in both eyes, Fig. 8(B-C), 7(F-G)). Importantly, the capillary defect map (Fig. 8(D) and 8(H)) clearly showed
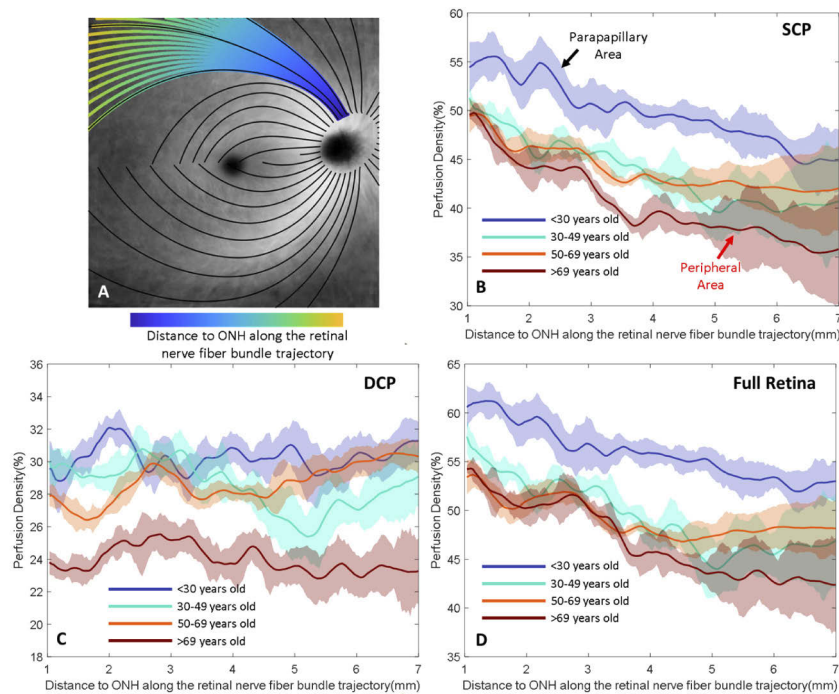
Fig. 7. Perfusion density distribution along the retinal nerve fiber trajectories. A) Overlaid retinal perfusion density map (grayscale) and simulated trajectories based on a mathematical model [26,27]. Finer retinal nerve fiber trajectories were plotted within 1-degree separation and the distance to the ONH along the nerve fiber trajectories was calculated and represented in *parula* color scale. B-D) Perfusion density distribution of superficial capillary plexus (SCP), deep capillary plexus (DCP), and full retina along retinal nerve fiber trajectories in four age groups. Solid curves and the semi-transparent bands represented the mean and the SD of perfusion along the trajectories.

the defect boundaries and the severities. The high values around the ONH were the artifacts because of the ONH size difference.

Structural information from OCT demonstrated high sensitivity and specificity in diagnosing glaucoma in the early stage [39,40], and the RNFL thickness decrease was along the nerve fiber bundle trajectories. Traditional 6×6 mm macular or ONH scans can only visualize part of the injured area, and provide an incomprehensive characterization of the glaucomatous damage. Our data confirmed the value of OCT scans in glaucoma diagnosis, and microvascular changes could provide information of early nutrients supply insufficiency to the neurons. Whether microvascular based diagnosis overperforms RNFL thickness based diagnosis remains unknown. The hypothesis that combining wide-field microvascular and morphological information increases the diagnostic power of early-stage glaucoma detection needs further investigation with larger clinical datasets.

Two representative eyes from two male patients (age: 64 & 72 years old) illustrated the usefulness of the normative database in moderate NPDR. Standard 35-degree fundus views showed clear evidence of hemorrhages (Fig. 8(I), white arrow) and soft exudate (Fig. 8(P), yellow arrow). In the OCTA images (SSI: 8 in both eyes, SCP: Fig. 8(J) and 8(Q); DCP: Fig. 8(M) and 8(T)), two types of microvascular changes could be observed: focal capillary dropout adjacent to large retinal vessels; diffuse capillary change associated with a lower OCTA signal. Blood flow rate is strongly correlated with the OCTA signal, although non-linearly [41], so a reduced OCTA signal might indicate a dysfunction of the capillary wall or pericytes, which occurs before the
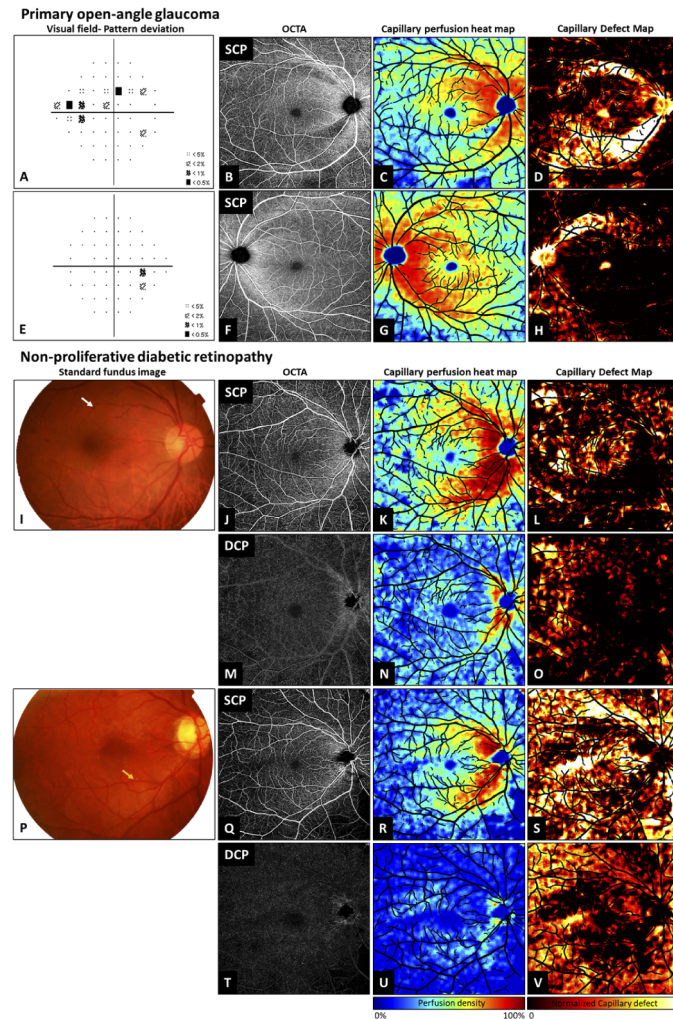
Fig. 8. Demonstration of using normative capillary perfusion maps in quantifying capillary defects in POAG eyes and NPDR eyes. A,E) Visual fields in POAG. B,F) 12×12 mm OCTA images in POAG eyes (Male, Age: 38, SSI: 10). I,P) Standard 35-degree fundus views. J,M) 12×12 mm OCTA images in moderate NDPR eye (Male, Age: 64, SSI: 8). Q,T) 12×12 mm OCTA images in moderate NDPR eye (Male, Age: 70, SSI: 8). The original grayscale OCTA images (second column) were processed by the methods to create capillary perfusion maps (third column). Their comparisons with age-matched normative capillary maps (fourth column) showed both the loci and severities of the capillary defects.

collapse or absence of the capillaries [42]. The capillary perfusion heatmaps (SCP: Fig. 8(K) and 8(R), DCP: Fig. 8(N) and 8(U)) provided direct views of the distribution of the capillaries. Alterations to the large vessels were less obvious at this stage and isolating them could augment our detection sensitivity on the microvascular changes [6]. Comparing with the age-matched normative database could simultaneously identify the loci and severities of the capillary dropout, especially in DCP. In the first case, some focal capillary defects and diffuse capillary change were detected in the peripheral and macular regions, respectively. In the macular region, DCP was less affected than SVP, while perfusion in both slabs were reduced in the retinal periphery (Fig. 8(L) and 8(O)). In the second case, despite focal capillary defects, the overall retinal perfusion was significantly lower than the normal distribution, on both SCP and DCP (Fig. 8(S) and 8(V)). Again, further investigation using larger clinical datasets will be needed for the clinical validation of our approach. These capillary defect maps have the potential to accurately quantify capillary drop out on consecutive visits to provide an additional measure for monitoring of peripheral vascular perfusion in eyes not only with early diabetic disease but also the therapeutic response of eyes undergoing treatment for proliferative diabetic retinopathy or diabetic macular edema.

Lastly, a total of 10 POAG eyes and 10 NPDR eyes were included to show their deviations for the normal distributions. The perfusion density in the entire 12×12 mm FOV, as well as the central 6×6 mm and the remaining square annulus, were evaluated, summarized in Table 2. As expected, significant differences in capillary perfusion were detected between the diseased eyes and the normal subjects, while the DCP were less affected. The sensitivity and specificity of using the normative database to classify POAG or NPDR needs to be done in larger datasets.

Table 2. Retinal perfusion density in healthy and diseased eyes

	Entire Field of View (12×12 mm)			Central Field of View (6×6 mm)			Square Annulus		
	SCP	DCP	Total Retinal	SCP	DCP	Total Retinal	SCP	DCP	Total Retinal
Normal subjects									
Group 1 (<30 yrs old) (n=24, OS/OD = 13/11)	56.51 ±4.95	29.02 ±7.63	60.68 ±4.72	66.01 ±3.55	25.89 ±10.09	67.22 ±3.57	53.22 ±5.80	30.09 ±7.10	58.42 ±5.66
Group 2 (30-49 yrs old) (n=28, OS/OD = 14/14)	51.60 ±6.01	26.36 ±6.82	54.94 ±6.87	60.88 ±6.49	25.73 ±7.89	61.75 ±7.82	48.41 ±6.70	26.58 ±7.15	52.60 ±7.57
Group 3 (50-69 yrs old) (n=109, OS/OD = 55/54)	51.47 ±7.28	25.89 ±9.84	54.19 ±7.95	60.08 ±8.20	24.28 ±10.34	60.27 ±8.78	48.52 ±7.53	26.44 ±9.89	52.10 ±8.32
Group 5 (>70 yrs old) (n=34, OS/OD = 19/15)	48.33 ±10.26	22.01 ±11.09	51.91 ±13.77	57.07 ±10.76	20.66 ±10.31	57.85 ±13.21	45.33 ±10.39	22.48 ±11.65	49.87 ±14.30
Combined vn(n = 195, OS/OD = 101/94)	51.56 ±7.76	25.66 ±9.59	54.70 ±9.09	60.40 ±8.39	24.05 ±10.06	60.92 ±9.46	48.52 ±8.04	26.22 ±9.75	52.56 ±9.53
POAG (n=10)	45.51 ±6.42	22.36 ±6.06	47.32 ±7.22	53.95 ±7.14	22.48 ±9.39	53.49 ±7.87	42.61 ±6.74	22.34 ±5.51	45.22 ±7.82
p-value	0.047	0.3420	0.082	0.072	0.211	0.052	0.061	0.074	0.043
NPDR (n=10)	40.43 ±6.60	21.83 ±7.22	41.95 ±7.21	45.92 ±8.21	22.99 ±5.71	48.03 ±7.72	38.58 ±7.16	21.44 ±7.86	39.88 ±7.75
p-value	0.006	0.245	<0.001	0.002	0.841	<0.001	0.017	0.172	<0.001

One limitation of this study is to use a commercially available prototype (PlexElite 9000) while OCTA images can be affected by multiple factors, including sampling frequency, optical resolution, and processing algorithms. Without knowing the parameters and algorithms, comparing OCTA

metrics from different machines needs caution. Furthermore, OCTA images, especially wider OCTA images were subjects to artifacts, such as motion artifact, shadow/projection artifacts [1,43,44]. Further investigation is needed to evaluate how these artifacts influence normative database, as well as its application in diseased eyes. Lastly, some confounders including blood pressure and intraocular pressure were not corrected. Magnification correction was not applied because of lacking eye length data. Magnification correction affects the perfusion density calculation [45], which is linearly correlated with the axial eye length. However, we partially mitigated this problem by registering the images according to the distance between centers of ONH and fovea, assuming a small individual variation of this distance [46].

4. Conclusions

In this study, we developed a normative database for 12×12 mm OCTA. We used a U-Net based deep learning algorithm to accurately segment the large blood vessels; the capillaries were consequently segmented by a moving window scheme. A total of 195 eyes were included and divided into 4 age groups: < 30 (N=24), 30-49 years old (N = 28), 50-69 (N=109) and >69 (N=34). Eyes with POAG and NPDR were used to demonstrate the usefulness of the normative database. Further investigations include evaluating the normative database on diagnosing pathological eyes in larger datasets.

Disclosures. The authors declare that there are no conflicts of interest related to this article.

Data availability. Data underlying the results presented in this paper are not publicly available at this time but may be obtained from the authors upon reasonable request.

Supplemental document. See Supplement 1 for supporting content.

References

1. J. Chua, B. Tan, M. Ang, M. E. Nongpiur, A. C. S. Tan, R. P. Najjar, D. Milea, and L. Schmetterer, "Future clinical applicability of optical coherence tomography angiography," Clin. Exp. Optom. **102**(3), 260–269 (2019).
2. R. F. Spaide, J. G. Fujimoto, N. K. Waheed, S. R. Sadda, and G. Staurenghi, "Optical coherence tomography angiography," Prog. Retinal Eye Res. **64**, 1–55 (2018).
3. C.-L. Chen and R. K. Wang, "Optical coherence tomography based angiography [Invited]," Biomed. Opt. Express **8**(2), 1056 (2017).
4. K. Y. Tey, K. Teo, A. C. S. Tan, K. Devarajan, B. Tan, J. Tan, L. Schmetterer, and M. Ang, "Optical coherence tomography angiography in diabetic retinopathy: a review of current applications," Eye Vis. **6**(1), 37 (2019).
5. G. D. Aaker, D. J. D'Amico, M. M. Wessel, G. Parlitsis, S. Kiss, and M. Cho, "Ultra–wide-field angiography improves the detection and classification of diabetic retinopathy," Retina **32**(4), 785–791 (2012).
6. B. Tan, J. Chua, E. Lin, J. Cheng, A. Gan, X. Yao, D. W. K. Wong, C. Sabanayagam, D. Wong, C. M. Chan, T. Y. Wong, L. Schmetterer, and G. S. Tan, "Quantitative microvascular analysis with wide-field optical coherence tomography angiography in eyes with diabetic retinopathy," JAMA Netw. open **3**(1), e1919469 (2020).
7. Q. Zhang, K. A. Rezaei, S. S. Saraf, Z. Chu, F. Wang, and R. K. Wang, "Ultra-wide optical coherence tomography angiography in diabetic retinopathy," Quant. Imaging Med. Surg. **8**(8), 743–753 (2018).
8. T. E. de Carlo, A. Romano, N. K. Waheed, and J. S. Duker, "A review of optical coherence tomography angiography (OCTA)," Int. J. Retin. Vitr. **1**(1), 5 (2015).
9. N. Choudhry, J. S. Duker, K. B. Freund, S. Kiss, G. Querques, R. Rosen, D. Sarraf, E. H. Souied, P. E. Stanga, G. Staurenghi, and S. V. R. Sadda, "Classification and Guidelines for Widefield Imaging: Recommendations from the International Widefield Imaging Study Group," Ophthalmol. Retin. **3**(10), 843–849 (2019).
10. F. Coscas, A. Sellam, A. Glacet-Bernard, C. Jung, M. Goudot, A. Miere, and E. H. Souied, "Normative data for vascular density in superficial and deep capillary plexuses of healthy adults assessed by optical coherence tomography angiography," Invest. Ophthalmol. Visual Sci. **57**(9), OCT211–OCT223 (2016).
11. J. I. Fernández-Vigo, B. Kudsieh, H. Shi, P. Arriola-Villalobos, J. Donate-López, J. García-Feijóo, J. M. Ruiz-Moreno, and J. Fernández-Vigo, "Normative database and determinants of macular vessel density measured by optical coherence tomography angiography," Clin. Exp. Ophthalmol. **48**(1), 44–52 (2020).

12. J. I. Fernández-Vigo, B. Kudsieh, H. Shi, L. De-Pablo-Gómez-de-Liaño, I. Serrano-Garcia, J. M. Ruiz-Moreno, J. M. Martínez-de-la-Casa, J. García-Feijóo, and J. ngel Fernández-Vigo, "Normative database of peripapillary vessel density measured by optical coherence tomography angiography and correlation study," Curr. Eye Res. **45**(11), 1430–1437 (2020).

13. Z. Zhi, Y. Jung, and R. K. Wang, "Label-free 3D imaging of microstructure, blood, and lymphatic vessels within tissue beds in vivo," Opt. Lett. **37**(5), 812 (2012).

14. O. Ronneberger, P. Fischer, and T. Brox, "U-net: Convolutional networks for biomedical image segmentation," in *Lecture Notes in Computer Science* (Including Subseries Lecture Notes in Artificial Intelligence and Lecture Notes in Bioinformatics) (2015).

15. J. D. Rodríguez, A. Pérez, and J. A. Lozano, "Sensitivity analysis of k-fold cross validation in prediction error estimation," IEEE Trans. Pattern Anal. Mach. Intell. **32**(3), 569–575 (2010).

16. R. F. Frangi, W. J. Niessen, K. L. Vincken, and M. A. Viergever, "Multiscale vessel enhancement filtering," Med. Image Comput. Comput. Assist. Interv. **1496**, 130–137 (1998).

17. E. Bekkers, R. Duits, T. Berendschot, and B. Ter Haar Romeny, "A multi-orientation analysis approach to retinal vessel tracking," J. Math. Imaging Vis. **49**(3), 583–610 (2014).

18. A. Longo, S. Morscher, J. M. Najafababdi, D. Jüstel, C. Zakian, and V. Ntziachristos, "Assessment of hessian-based Frangi vesselness filter in optoacoustic imaging," Photoacoustics **20**, 100200 (2020).

19. B. Tan, A. Wong, and K. Bizheva, "Enhancement of morphological and vascular features in OCT images using a modified Bayesian residual transform," Biomed. Opt. Express **9**(5), 2394 (2018).

20. T. T. Nguyen and T. Y. Wong, "Retinal vascular changes and diabetic retinopathy," Curr. Diab. Rep. **9**(4), 277–283 (2009).

21. J. Yu, R. Gu, Y. Zong, H. Xu, X. Wang, X. Sun, C. Jiang, B. Xie, Y. Jia, and D. Huang, "Relationship between retinal perfusion and retinal thickness in healthy subjects: An optical coherence tomography angiography study," Invest. Ophthalmol. Visual Sci. **57**(9), OCT204–OCT210 (2016).

22. Y. C. Tham, C. Y. Cheng, Y. Zheng, T. Aung, T. Y. Wong, and C. Y. Cheung, "Relationship between retinal vascular geometry with retinal nerve fiber layer and ganglion cell-inner plexiform layer in nonglaucomatous eyes," Invest. Ophthalmol. Visual Sci. **54**(12), 7309–7316 (2013).

23. P. E. Z. Tan, C. Balaratnasingam, J. Xu, Z. Mammo, S. X. Han, P. Mackenzie, A. W. Kirker, D. Albiani, A. B. Merkur, and M. V. Sarunic, "Quantitative comparison of retinal capillary images derived by speckle variance optical coherence tomography with histology," Invest. Ophthalmol. Vis. Sci. **56**(6), 3989–3996 (2015).

24. D. Y. Yu, S. J. Cringle, P. K. Yu, C. Balaratnasingam, A. Mehnert, M. V. Sarunic, D. An, and E. N. Su, "Retinal capillary perfusion: Spatial and temporal heterogeneity," Prog. Retinal Eye Res. **70**, 23–54 (2019).

25. K. Pappelis and N. M. Jansonius, "Quantification and repeatability of vessel density and flux as assessed by optical coherence tomography angiography," Transl. Vis. Sci. Technol. **8**(3), 3 (2019).

26. H. L. Rao, Z. S. Pradhan, R. N. Weinreb, H. B. Reddy, M. Riyazuddin, S. Dasari, M. Palakurthy, N. K. Puttaiah, D. A. S. Rao, and C. A. B. Webers, "Regional comparisons of optical coherence tomography angiography vessel density in primary open-angle glaucoma," Am. J. Ophthalmol. **171**, 75–83 (2016).

27. Y. Wei, H. Jiang, Y. Shi, D. Qu, G. Gregori, F. Zheng, T. Rundek, and J. Wang, "Age-related alterations in the retinal microvasculature, microcirculation, and microstructure," Invest. Ophthalmol. Visual Sci. **58**(9), 3804–3817 (2017).

28. Y. Lin, H. Jiang, Y. Liu, G. R. Gameiro, G. Gregori, C. Dong, T. Rundek, and J. Wang, "Age-related alterations in retinal tissue perfusion and volumetric vessel density," Invest. Ophthalmol. Visual Sci. **60**(2), 685–693 (2019).

29. N. M. Jansonius, J. Nevalainen, B. Selig, L. M. Zangwill, P. A. Sample, W. M. Budde, J. B. Jonas, W. A. Lagrèze, P. J. Airaksinen, R. Vonthein, L. A. Levin, J. Paetzold, and U. Schiefer, "A mathematical description of nerve fiber bundle trajectories and their variability in the human retina," Vision Res. **49**(17), 2157–2163 (2009).

30. N. M. Jansonius, J. Schiefer, J. Nevalainen, J. Paetzold, and U. Schiefer, "A mathematical model for describing the retinal nerve fiber bundle trajectories in the human eye: average course, variability, and influence of refraction, optic disc size and optic disc position," Exp. Eye Res. **105**, 70–78 (2012).

31. J. Hong, B. Tan, N. D. Quang, P. Gupta, E. Lin, D. Wong, M. Ang, E. Lamoureux, L. Schmetterer, and J. Chua, "Intra-session repeatability of quantitative metrics using widefield optical coherence tomography angiography (OCTA) in elderly subjects," Acta Ophthalmol. **98**(5), 570–578 (2020).

32. A. Zhang, Q. Zhang, C.-L. Chen, and R. K. Wang, "Methods and algorithms for optical coherence tomography-based angiography: a review and comparison," J. Biomed. Opt. **20**(10), 100901 (2015).

33. A. Camino, P. Zang, A. Athwal, S. Ni, Y. Jia, D. Huang, and Y. Jian, "Sensorless adaptive-optics optical coherence tomographic angiography," Biomed. Opt. Express **11**(7), 3952–3967 (2020).

34. B. Tan, R. Sim, J. Chua, D. W. Wong, X. Yao, G. Garhöfer, D. Schmidl, L. Werkmeister, and R. M. Schmetterer, "Approaches to quantify OCTA metrics," Ann. Transl. Med. **8**(18), 1205 (2020).

35. A. M. Bata, K. Fondi, S. Szegedi, G. C. Aschinger, A. Hommer, D. Schmidl, J. Chua, R. M. Werkmeister, G. Garhöfer, and L. Schmettere, "Age-Related Decline of Retinal Oxygen Extraction in Healthy Subjects," Invest. Ophthalmol. Visual Sci. **60**(8), 3162–3169 (2019).

36. M. A. Samuel, Y. Zhang, M. Meister, and J. R. Sanes, "Age-related alterations in neurons of the mouse retina," J. Neurosci. **31**(44), 16033–16044 (2011).

37. X. DIng, R. T. Chang, X. Guo, X. Liu, C. A. Johnson, B. A. Holden, and M. He, "Visual field defect classification in the Zhongshan Ophthalmic Center-Brien Holden Vision Institute High Myopia Registry Study," Br. J. Ophthalmol. **100**(12), 1697–1702 (2016).
38. R. P. Mills, D. L. Budenz, P. P. Lee, R. J. Noecker, J. G. Walt, L. R. Siegartel, S. J. Evans, and J. J. Doyle, "Categorizing the stage of glaucoma from pre-diagnosis to end-stage disease," Am. J. Ophthalmol. **141**(1), 24–30 (2006).
39. D. C. Hood, N. De Cuir, D. M. Blumberg, J. M. Liebmann, R. Jarukasetphon, R. Ritch, and C. G. De Moraes, "A single wide-field OCT protocol can provide compelling information for the diagnosis of early glaucoma," Transl. Vis. Sci. Technol. **5**(6), 4 (2016).
40. K. Wu, C. Lin, A. K. N. Lam, L. Chan, and C. Kai-Shun Leung, "Wide-field trend-based progression analysis of combined retinal nerve fiber layer and ganglion cell inner plexiform layer thickness: a new paradigm to improve glaucoma progression detection," Ophthalmology **127**(10), 1322–1330 (2020).
41. S. B. Ploner, E. M. Moult, W. Choi, N. K. Waheed, B. Lee, E. A. Novais, E. D. Cole, B. Potsaid, L. Husvogt, J. Schottenhamml, A. Maier, P. J. Rosenfeld, J. S. Duker, J. Hornegger, and J. G. Fujimoto, "Toward quantitative optical coherence tomography angiography," Retina **36**(Supplement 1), S118–S126 (2016).
42. C. Rask-Madsen and G. L. King, "Vascular complications of diabetes: Mechanisms of injury and protective factors," Cell Metab. **17**(1), 20–33 (2013).
43. E. A. T. Say, S. Ferenczy, G. N. Magrath, W. A. Samara, C. T. L. Khoo, and C. L. Shields, "Image quality and artifacts on optical coherence tomography angiography," Retina **37**(9), 1660–1673 (2017).
44. A. Camino, M. Zhang, S. S. Gao, T. S. Hwang, U. Sharma, D. J. Wilson, D. Huang, and Y. Jia, "Evaluation of artifact reduction in optical coherence tomography angiography with real-time tracking and motion correction technology," Biomed. Opt. Express **7**(10), 3905–3915 (2016).
45. D. M. Sampson, P. Gong, D. An, M. Menghini, A. Hansen, D. A. Mackey, D. D. Sampson, and F. K. Chen, "Axial length variation impacts on superficial retinal vessel density and foveal avascular zone area measurements using optical coherence tomography angiography," Invest. Ophthalmol. Visual Sci. **58**(7), 3065–3072 (2017).
46. H. Kim, J. S. Lee, H. M. Park, H. Cho, H. W. Lim, M. Seong, J. Park, and W. J. Lee, "A wide-field optical coherence tomography normative database considering the fovea-disc relationship for glaucoma detection," Transl. Vis. Sci. Technol. **10**(2), 7 (2021).